FRONTIERS OF PHYSICS

RESEARCH ARTICLE
Volume 18 / Issue 1 / 13304 / 2023

Emerging weak antilocalization effect in $Ta_{0.7}Nb_{0.3}Sb_2$ semimetal single crystals

Meng Xu[1,2], Lei Guo[2,†], Lei Chen[3], Ying Zhang[4], Shuang-Shuang Li[4], Weiyao Zhao[5,‡], Xiaolin Wang[6], Shuai Dong[2], Ren-Kui Zheng[4,§]

1 College of Science, Hohai University, Nanjing 210098, China
2 School of Physics, Southeast University, Nanjing 211189, China
3 School of Physics and Materials Science, Guangzhou University, Guangzhou 510006, China
4 School of Materials Science and Engineering, Jiangxi Engineering Laboratory for Advanced Functional Thin Films, Nanchang University, Nanchang 330031, China
5 Department of Materials Science & Engineering, Monash University, Clayton 3800 VIC, Australia
6 Institute for Superconducting and Electronic Materials, & ARC Centre of Excellence in Future Low-Energy Electronics Technologies, Innovation Campus, University of Wollongong, North Wollongong NSW 2500, Australia
Corresponding authors. E-mail: †leiguo@seu.edu.cn, ‡weiyao.zhao@monash.edu, §zrk@ustc.edu
Received April 2, 2022; accepted July 27, 2022

© Higher Education Press 2023

ABSTRACT

Weak antilocalization (WAL) effect is commonly observed in low-dimensional systems, three-dimensional (3D) topological insulators and semimetals. Here, we report the growth of high-quality $Ta_{0.7}Nb_{0.3}Sb_2$ single crystals via the chemical vapor transport (CVT). Clear sign of the WAL effect is observed below 50 K, probably due to the strong spin–orbital coupling in 3D bulk. In addition, it is worth noting that a relatively large MR of 120% appears under 1 T magnetic field at $T = 2$ K. Hall measurements and two-band model fitting results reveal high carrier mobility (>1000 $cm^2 \cdot V^{-1} \cdot s^{-1}$ in 2–300 K region), and off-compensation electron/hole ratio of ~8:1. Due to the angular dependence of the WAL effect and the fermiology of the $Ta_{0.7}Nb_{0.3}Sb_2$ crystals, interesting magnetic-field-induced changes of the symmetry of the anisotropic magnetoresistance (MR) from two-fold (≤ 0.6 T) to four-fold (0.8–1.5 T) and finally to two-fold (≥ 2 T) are observed. This phenomenon is attributed to the mechanism shift from the low-field WAL dominated MR to WAL and fermiology co-dominated MR and finally to high-field fermiology dominated MR. All these signs indicate that $Ta_{0.7}Nb_{0.3}Sb_2$ may be a topological semimetal candidate, and these magnetotransport properties may attract more theoretical and experimental exploration of the $(Ta,Nb)Sb_2$ family.

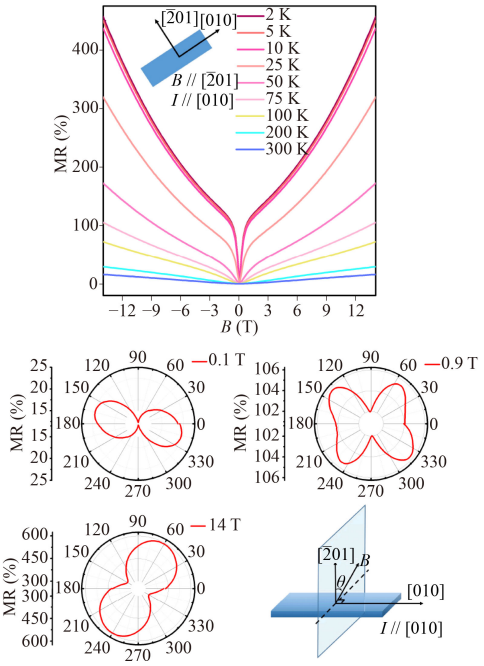

Keywords topological semimetal, magnetoresistance, weak antilocalization effect, spin–orbital coupling

1 Introduction

Topological insulators and semimetals with unique band topology are the focus of condensed matter physics in recent years. Due to their extraordinary topological surface state and special Fermi surfaces, these topological materials show many quantum phenomena such as extreme large magnetoresistance, ultrahigh carrier

https://doi.org/10.1007/s11467-022-1198-6

mobility, weak antilocalization (WAL) effect, quantum oscillation, quantized Hall effect, and chiral anomaly in magnetoresistance, which not only provides a broader platform for basic physics research, but also opens up a new way to explore the potential applications in spintronics and quantum computing [1–6].

The electronic transport properties of intermetallic compounds have been intensively studied in the past decade [1–6]. Among these compounds, the compensated semimetals of $M\mathrm{Sb}_2$ (M = Nb, Ta) with extremely large magnetoresistance (XMR) and low-temperature resistivity plateaus are attracting increasing attention [7–14]. Theoretical and experimental results show that the NbSb_2 and TaSb_2 are topological materials or good candidates. They could be weak topological insulators in the absence of magnetic field, and could be transformed into type-II Weyl semimetals with application of external magnetic fields [13, 14]. It is worth noting that the surface state and electronic properties of topological materials can be adjusted by doping or element replacement. A typical example is the type-II Weyl semimetals $\mathrm{Mo}_{1-x}\mathrm{W}_x\mathrm{Te}_2$ system [15–17]. Mo doping significantly expands the Fermi arc on its topological surface and greatly reduces the difficulty of direct observation of surface states by angle resolved photoelectron spectroscopy (ARPES). Similar to $\mathrm{Mo}_{1-x}\mathrm{W}_x\mathrm{Te}_2$ system, some interesting stories may occur in $\mathrm{Ta}_{1-x}\mathrm{Nb}_x\mathrm{Sb}_2$ system in which the regulation of topological state could be realized by doping between Nb and Ta [12].

Due to the high chemical similarity between these two compounds, the high-throughput one-pot crystal growth process based on chemical vapor transport (CVT) was recently explored [12] to grow a range of $\mathrm{Ta}_{1-x}\mathrm{Nb}_x\mathrm{Sb}_2$ ($0 \le x \le 1$) crystals within one silica tube, providing the possibility to investigate the exotic electronic transport behaviors of $\mathrm{Ta}_{1-x}\mathrm{Nb}_x\mathrm{Sb}_2$ ($0 \le x \le 1$) compounds. In our previous electronic transport study of the (Ta,Nb)Sb_2 family, we observed the carrier's-compensation-induced XMR effect in the Nb lightly doped $\mathrm{Ta}_{1-x}\mathrm{Nb}_x\mathrm{Sb}_2$ ($x \le 10\%$) and Ta lightly doped $\mathrm{Nb}_{1-x}\mathrm{Ta}_x\mathrm{Sb}_2$ ($x \le 10\%$) crystals [12]. For Ta-Nb equally mixed crystals ($x \sim 0.5$), the low-temperature magnetoresistance (MR) is drastically suppressed and the maximum MR value is only 80% at 2 K and 9 T due to the deviation from the optimal carriers' compensated region ($n_\mathrm{h}/n_\mathrm{e} \sim 1$). On the basis of the previous work, we continue to explore the possible effects of doping on the topological state of this system.

For the study of topological materials, the most common method is to extract the topological properties of surface state through electronic transport measurements such as giant magnetoresistance, SdH oscillation, and WAL effect. Due to the limitations of crystal quality, defects, impurities and existing magnetic field strength, it is difficult to detect SdH oscillation in many cases. On the other hand, WAL effect expressed as the positive correction of resistivity in the presence of a low magnetic field is easier to be detected. Due to the spin-momentum locking, the spin rotates along the backscattering path. At this time, the phase difference between the clockwise and counterclockwise trajectories reaches 360°, which further causes the change of the sign of the scattering amplitude, leads to the cancellation of the interference between the two scattering events, and ultimately suppress the occurrence of backscattering. That is, there is destructive interference between spin up and spin down carriers, resulting in cusp-like positive magnetoconductance behaviors, and the electron spin and orbital coherence can be destroyed by the external magnetic field in the whole process [18, 19]. As a result, the WAL effects are usually observed in low-dimensional systems such as 2D materials of graphene, thin films of $\mathrm{Na}_2\mathrm{IrO}_3$, $\mathrm{In}_2\mathrm{O}_3$, and thin flakes of MoTe_2 [20–23] due to higher scattering occurrence between two time-reversed paths. As for the 3D systems, WAL effect is uncommon and usually originates from either strong spin-orbit interaction in the bulk and/or spin-momentum locking in the topological surface states. The topological nontrivial band structure is closely related to strong spin-orbit coupling in topological materials, thus WAL effect can also be observed in some specific three-dimensional systems. A special system that exhibits WAL effect is 3D topological insulators ($\mathrm{Bi}_2\mathrm{Se}_3$, $\mathrm{Bi}_2\mathrm{Te}_3$, $\mathrm{Bi}_2\mathrm{Te}_2\mathrm{Se}$, $\mathrm{Bi}_2\mathrm{Se}_{2.1}\mathrm{Te}_{0.1}$, V_x:$\mathrm{Bi}_{1.08-x}\mathrm{Sn}_{0.02}\mathrm{Sb}_{0.9}\mathrm{Te}_2\mathrm{S}$, etc.), where the spin-moment locking of topologically protected surface states provide the source of destructive interference [24–28]. Recently, WAL effect is also reported in some 3D topological semimetal single crystals (LuPdBi [29, 30], ScPtBi [31], YbCdGe [32], YbCdSn [33], CaAgBi [34]), topological superconductors (LuPdBi [29, 30]), and a very small number of half-Heusler compounds (ScPdBi [35], ScNiBi [36], LuNiBi [37], LuPtSb [38]). Considering the huge variety of 3D materials, the WAL effect in these 3D materials are still very rare. Experimentally, WAL effect can be detected by measuring the magnetoconductance at low temperatures, and normally could be explained within the Hikami–Larkin–Nagaoka (HLN) model [39, 40].

In this work, we observed WAL effect in CVT-grown high quality $\mathrm{Ta}_{0.7}\mathrm{Nb}_{0.3}\mathrm{Sb}_2$ single crystals at low temperatures. The magnetotransport properties of the $\mathrm{Ta}_{0.7}\mathrm{Nb}_{0.3}\mathrm{Sb}_2$ crystals are similar to those of previously reported TaSb_2, NbSb_2 and (Ta,Nb)Sb_2, e.g., large, non-saturating MR, resistivity plateaus below 10 K, and magnetic field induced resistivity upturn. The very different point is that at low temperatures, the MR curves show sharp "V" shape below 1 T magnetic field and increase parabolically with the magnetic fields above 1 T. The WAL shape of MR curve survives up to ~ 50 K, which can be quite well fitted via the HLN model. Due to the different angular dependence of WAL effect and the fermiology of $\mathrm{Ta}_{0.7}\mathrm{Nb}_{0.3}\mathrm{Sb}_2$, the symmetry of angular MR evolves with magnetic field. All of these results make $\mathrm{Ta}_{0.7}\mathrm{Nb}_{0.3}\mathrm{Sb}_2$ single crystals a good platform for the fundamental research of (Ta,Nb)Sb_2 family or other similar semimetal systems.

2 Experimental sections

$Ta_{0.7}Nb_{0.3}Sb_2$ single crystals were grown via the CVT method. Briefly, a total amount of about 1.0 g of high-purity Nb (99.95%, aladdin), Ta (99.9%, aladdin), and Sb (99.9999%, aladdin) powders, together with 0.15 g I_2 granules were sealed in a quartz tube with the pressure less than 10^{-3} Pa. The crystal growth took place in a two-zone furnace from 1000 °C (source) to 1100 °C (sink) for 10 days before cooling naturally to room temperature. Finally, typical prismatic single crystals with a size of about 2 mm × 1 mm × 0.5 mm were successfully obtained [Fig. 1(a)].

The crystallographic orientation of the major surface of the $Ta_{0.7}Nb_{0.3}Sb_2$ was characterized by XRD (Rigaku SmartLab). Energy Dispersive X-ray Spectroscopy (EDS) (Oxford Aztec X-Max80) measurements show the good stoichiometry and uniformity distribution of the constituent elements of the $Ta_{0.7}Nb_{0.3}Sb_2$ single crystals. In addition, the high-resolution transmission electron microscopy (HRTEM) and selected area electron diffraction (SAED) patterns measurements were performed using a Tecnai G2F20 S-Twin microscope to analyze the structure and crystallinity of the crystals.

Finally, using physical properties measurement system (PPMS-14 T, Quantum Design), the electronic transport properties of $Ta_{0.7}Nb_{0.3}Sb_2$ crystals were measured via the four-probe and six-probe methods, respectively. During the measurements, the electric current direction is always along the *b*-axis of the crystal, and the initial direction of the magnetic field is along the $[\bar{2}01]$ direction of the crystal [see inset of Fig. 2(a)].

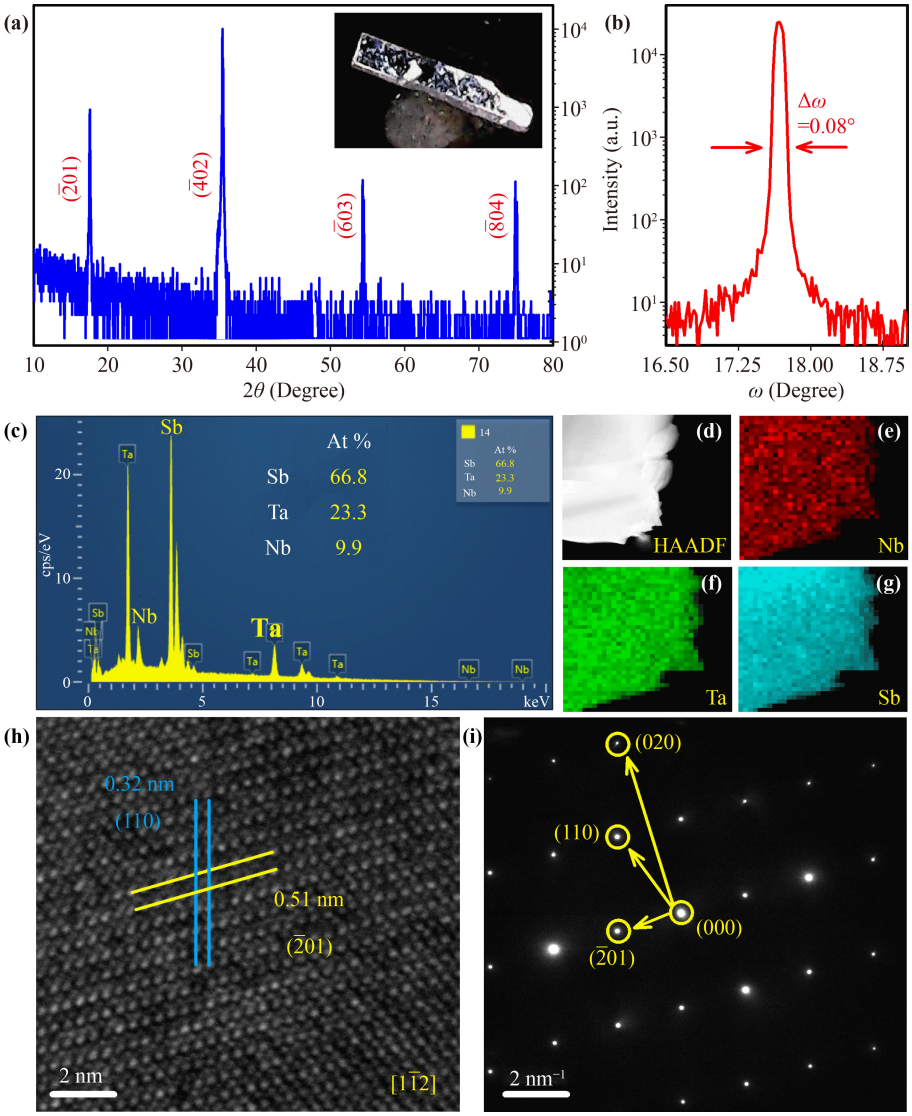

Fig. 1 **(a)** XRD pattern of the $Ta_{0.7}Nb_{0.3}Sb_2$ single crystal. Inset: An optical image of the crystal. **(b)** XRD rocking curve taken on the $(\bar{4}02)$ diffraction peak. **(c–g)** The element spectrum and element mapping patterns of the $Ta_{0.7}Nb_{0.3}Sb_2$ single crystal. **(h)** HRTEM image. **(i)** SAED pattern.

3 Results and discussion

As shown in the inset of Fig. 1(a), the $Ta_{0.7}Nb_{0.3}Sb_2$ single crystal shows rod-like shape, with its length direction along the [010] direction of the crystal and mirror-like major surface with its normal vector along the [$\bar{2}$01] direction. To examine the crystal structure, XRD measurements were carried out on the shiny plane of the selected single crystal. The sharp comb-like ($h0l$) (h = –2, –4, –6, –8; $l = h/2$) diffraction pattern [Fig. 1(a)] and small full width at half maximum (FWHM) (~ 0.08°) of the ($\bar{4}$02) diffraction peak [Fig. 1(b)] confirm the high quality of the $Ta_{0.7}Nb_{0.3}Sb_2$ crystal. As reported previously, $Ta_{1-x}Nb_xSb_2$ ($0 < x < 1$) compounds share the same monoclinic structure ($C_{12/m1}$ space group) with the MSb_2 (M = Ta, Nb) parent compounds [7, 12, 41].

We carried out EDS measurements on the major surface of the crystal to determine its chemical composition and element distribution. As shown in Fig. 1(c), the Ta, Nb, and Sb elements and their atomic ratio is 23.3%: 9.9%:66.8%, which is close to the nominal stoichiometry of $Ta_{0.7}Nb_{0.3}Sb_2$. In addition, we carried out elemental analysis of a milled sample with the help of TEM. As shown in Figs. 1(e)–(g), the elements of Ta, Nb and Sb distribute evenly. Besides, the HRTEM image demonstrates that its lattice spacing of the ($\bar{2}$01) and (110) planes are 0.51 and 0.32 nm, respectively [Fig. 1(h)], which is in agreement with the monoclinic structure characteristics given by XRD [41]. The excellent microstructure results in sharp SAED pattern [Fig. 1(i)]. All these results make $Ta_{0.7}Nb_{0.3}Sb_2$ a reliable platform for studying its electronic transport properties.

As displayed in Figs. 2(a) and (b), the zero-field resistivity of the $Ta_{0.7}Nb_{0.3}Sb_2$ crystal increases monotonically with increasing temperature from 2 K to 300 K, showing the typical metallic characteristics. The resistivity is approximately 18 μΩ·cm at 2 K, further suggesting its good metallic conductivity, which could be attributed to the large mean free path of the electrons [42]. For zero field, the residual resistivity ratio (RRR) is approximately 10.6. In addition, the resistivity at temperature region of 2–30 K can be well described by the formula $\rho(T) = \rho_0 + AT^n$ with $n \sim 2.3$, where ρ_0 represents the residual resistivity, A is a fitting constant, and n is a parameter suggesting scattering mechanisms. The values of n is smaller than semimetals like LaBi ($n = 3$) [43], LaSb ($n = 4$) [44], ZrGeSe ($n = 3.1$) [45] whose scattering mechanism is attributed to electron-phonon scattering and deviates from the pure electronic correlation-dominated scattering mechanism ($n = 2$) [46, 47]. So we speculate that at the low temperature region, this temperature dependence of resistivity probably originates from the coexistence and competition of these two scattering mechanisms.

For the magnetic field $B \geq 1$ T, a metal-insulator transition and a resistivity plateau (the grey shadow areas) occur at low temperature [Fig. 2(b)], both of which are positively correlated with the magnetic field strength. These resistivity behaviors are generic features of topological semimetals [32, 33, 42–45]. To further analyze these features, we plot first derivative of the resistivity [$(\partial\rho_{xx}/\partial T)$] as a function of temperature in Fig. 2(c). Two characteristic temperatures can be determined from the figure: i) the metal-insulator transition temperature T_m, where $\partial\rho_{xx}/\partial T = 0$, as indicated by the red dotted line; ii) the onset temperature of the resistivity platform (T_i), corresponding to the minimum of $\partial\rho_{xx}/\partial T$, as indicated by the olive arrow. As displayed in the inset of Fig. 2(c), T_m increases monotonically with the magnetic field. The relationship between T_m and B can be well fitted into the formula $T_m \sim a(B–B_0)^{1/\nu}$ with $\nu \approx 1.96$, which is close to the values of compensated semimetals such as WTe_2 ($\nu = 2$) [47] and Bi ($\nu = 2$) [48]. For (Ta,Nb)Sb_2 crystals, the carriers are off-compensation within 10% < Nb percentage < 50% region. Therefore, the magnetic-field-induced resistivity upturn in the present $Ta_{0.7}Nb_{0.3}Sb_2$ single crystal with 30 atom% Nb are not as strong as that in the $TaSb_2$ [12] because of the off-compensation of the electron and hole carriers.

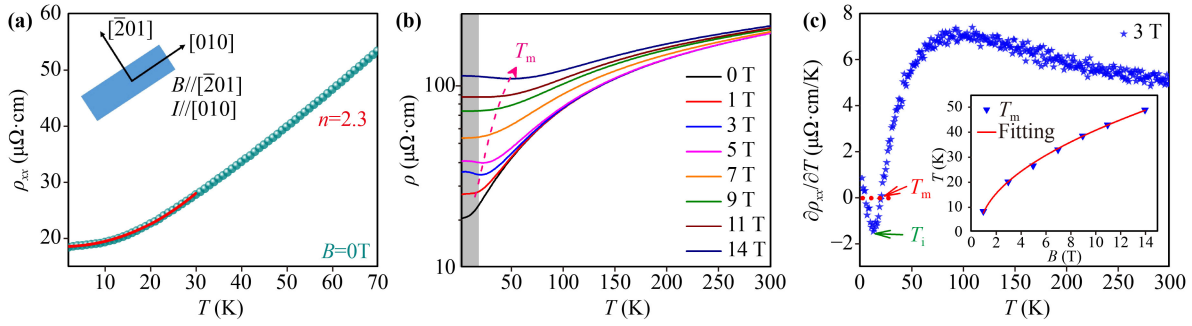

Fig. 2 **(a)** Zero-field resistivity (cyan points) and fitting results (red curve) of the $Ta_{0.7}Nb_{0.3}Sb_2$ single crystal. Inset: schematic geometry of the directions of the magnetic field and the electric current. **(b)** Temperature dependence of the resistivity under different magnetic fields, as measured using the schematic geometry shown in the inset of **(a)**. The grey shadow areas show the resistance plateau region and the pink dash arrow indicates the resistance minimum temperature (T_m). **(c)** $\partial\rho_{xx}/\partial T$ plotted as a function of temperature, taking $B = 3$ T as an example. Insert: T_m plotted as a function of the magnetic field B.

To further explore the carrier's properties of the $Ta_{0.7}Nb_{0.3}Sb_2$ crystal, we measured Hall resistivity (ρ_{xy}) at different temperatures ranging from 1.8 K to 300 K, which are plotted in Fig. 3(a). The nonlinear tendency of the ρ_{xy} versus B curves suggest the existence of multi-type carriers, especially at low temperatures and low field region. Here, we consider the semiclassical two band model to analyze the carrier's density & Hall mobility [46, 49]. The total conductivity tensor σ can be fitted into the plural form as follows:

$$\sigma = e\left(\frac{\mu_e n_e}{1+\mathrm{i}u_e B}+\frac{\mu_h n_h}{1-\mathrm{i}u_h B}\right), \tag{1}$$

where the subscripts e and h represent the electron and hole, respectively. n and μ denote the carrier density and mobility, respectively. The conductivity σ can be transformed to the resistivity tensor ρ using $\rho = \sigma^{-1}$ whose real and imaginary parts ρ_{xx} and ρ_{xy} can be calculated by

$$\begin{aligned}\rho_{xx}(B) =& \mathrm{Re}(\rho)\\ =& \frac{1}{e}\frac{(n_h\mu_h+n_e\mu_e)+(n_h\mu_e+n_e\mu_h)\mu_e\mu_h B^2}{(n_h\mu_h+n_e\mu_e)^2+(n_h-n_e)^2\mu_e{}^2\mu_h{}^2B^2},\end{aligned} \tag{2}$$

$$\begin{aligned}\rho_{xy}(B) =& \mathrm{Im}(\rho)\\ =& \frac{B}{e}\frac{(n_h\mu_h^2-n_e\mu_e^2)+(n_h-n_e)\mu_e^2\mu_h^2B^2}{(n_h\mu_h+n_e\mu_e)^2+(n_h-n_e)^2\mu_e{}^2\mu_h{}^2B^2}.\end{aligned} \tag{3}$$

The ρ_{xy} data were fitted by Eq. (3) [Fig. 3(b)] to obtain the fitting parameters n_e, n_h, μ_e, and μ_h. Figure 3(b) only shows four fitting curves (1.8, 30, 75 and 200 K) in the positive magnetic field region as representative in order to show the fitting clearly. The fitting parameters are plotted as a function of temperature in Fig. 3(c). The electron and hole densities n_e and n_h increase with temperature while the electron and hole mobilities show opposite variation trend for $T \le 100$ K. At 300 K, the Hall resistivity versus magnetic field curve is nearly a straight line with negative slope [Fig. 3(a)], where the hole carrier density is near 0. Overall, there are two important features of the Hall results: 1) the ratio n_e/n_h is about 8 at $T = 2$ K, which demonstrates the off-compensation of electron and hole carriers. 2) even at 300 K, the electron and hole mobility still remain at a relatively high value of ~1.1 × 10^3 $cm^2 \cdot V^{-1} \cdot s^{-1}$, which could contribute to the large MR effect. The high mobility within a wide temperature region up to room temperature may make it a promising candidate system for high efficiency electronic device applications.

Because of the high carrier's mobility, a sizeable MR effect is expected in the $Ta_{0.7}Nb_{0.3}Sb_2$ crystal. Transverse MR describes the relative change of resistivity when the magnetic field is applied vertically with respect to the direction of the electric current. MR usually refers to the relative change in resistivity in the presence of a magnetic field with respect to zero magnetic field. Therefore, MR is calculated by $\mathrm{MR} = \frac{\rho(B)-\rho(0)}{\rho(0)}$, where $\rho(B)$ and $\rho(0)$ refer to the resistivity at a magnetic field B and zero magnetic field, respectively. Figure 4(a) shows the variation of transverse MR with the magnetic field at a specific temperature. First, MR exhibits unsaturated quasi-parabolic behavior up to 14 T and the MR vs. B curves below 10 K almost coincide with each other, which is consistent with the resistivity plateau behaviors discussed above. For $T = 2$ K and $B = 14$ T, MR is 457 %, which is 1–2 orders of magnitude lower than that of the $TaSb_2$ and $NbSb_2$ parent compounds, but comparable to those of previously reported semimetals [30–33]. After Nb doping, the inter-valley scattering may be enhanced due to the increased atomic disorder. This, together with the shift of its Fermi level away from the compensation area, results in the decrease of MR upon Nb doping [12]. For $T \ge 50$ K, MR decreases remarkably with increasing temperature and finally reaches 15.7 % for $T = 300$ K and $B = 14$ T, which is quite similar to the situation of traditional metal materials.

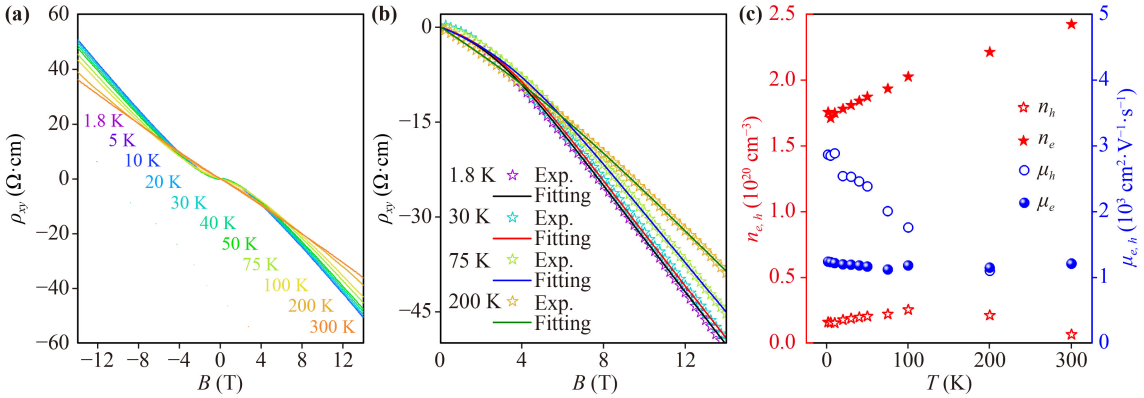

Fig. 3 **(a)** Hall resistivity as a function of the magnetic field at different fixed temperatures for the $Ta_{0.7}Nb_{0.3}Sb_2$ single crystal. **(b)** Double-band model fitting of the Hall resistivity versus magnetic field curves. **(c)** Temperature dependence of the carrier's density and mobility, obtained via the double-band fitting.

In the low-field (–0.5 T ≤ B ≤ 0.5 T) and low-temperature region (T < 50 K), MR versus B curves show a sharp cusp-like shape which is a typical phenomenon of WAL effect [18–20, 50]. We made more detailed measurements in the low field region to better understand these phenomena and show the results in Fig. 4(b). MR increases rapidly as the temperature decreases from 50 to 2 K, and reached a maximum value of 120% at B = 1 T and T = 2 K. Figure 4(c) shows the MR vs. B curves at 2 K, with the direction of the magnetic field tilting from [$\bar{2}$01], corresponding to a rotation of the crystal around the [010] axis. As schematically shown in Fig. 4(c), θ is the angle between the direction of the magnetic field and the [$\bar{2}$01] orientation and the direction of the magnetic field is always vertical to the electric current direction during the tilting process. Similar phenomena have been observed for all tilting angles in Fig. 4(c). Another point is that, during the rotation of the crystal, the MR value at B = 14 T first decreases to a minimum value at $\theta \sim 50°$, then increases. To further study this anisotropy MR effect, angular dependent MR is measured and will be discussed later.

As discussed above, MR displays a prominent cusp in the low-field region below 50 K which is the reminiscent of the WAL effect and is generally found in 3D systems with strong spin–orbital coupling (SOC) or two-dimensional (2D) topological insulators with nontrivial surface states [21–38]. Recently, the WAL effect has been observed in some 3D semimetal crystals, such as ScPtBi, YbCdGe, YbCdSn, CaAgBi, ScPdBi [31–35]. To investigate the origin of the WAL effect in the $Ta_{0.7}Nb_{0.3}Sb_2$ crystal, the HLN model is applied to analyze the 2D magnetoconductance which could be expressed as follows:

$$\Delta G(B) = G(B) - G(0) = \frac{\alpha e^2}{2\pi^2\hbar}\left[\Psi\left(\frac{1}{2}+\frac{\hbar}{4el_\phi^2 B}\right) - \ln\left(\frac{\hbar}{4el_\phi^2 B}\right)\right], \quad (4)$$

where $G(B)$ and $G(0)$ are the conductance with and without magnetic field, respectively. Ψ represents the digamma function, α = –1/2 per conduction channel, and l_ϕ is the phase coherence length, respectively [39–40]. Therefore, the value of α could be used to estimate the number of conducting channels. The WAL is generally observed in 2D topological materials and the HLN model can be applied directly to these 2D system. The parent compounds of (Ta,Nb)Sb_2 have been predicted to be weak topological semimetals [7–14], so it makes sense to study the origin of the WAL effect using the HLN model. However, ΔG of 3D systems is too large to be fitted directly by the HLN model due to the significant large thickness than 2D-like system. Throughout the MR measurements, the applied current is perpendicular to the thickness direction. Naturally, the conductance of 3D systems can be seen as an addition of the 2D conduction layers periodically stacked along the thickness direction. Therefore, ΔG that is going to be fitted by the HLN model should be divided by the number of 2D conduction layers Z*, which is about half of the quantum layer number, i.e., Z^* = 0.5 × t / (1 nm). Hence, we define the magnetoconductance per contributing 2D layer as: $\Delta\widetilde{G}(B) = \Delta G(B)/Z^*$, and fit $\Delta\widetilde{G}(B)$ using the HLN model [25, 27]. As shown in Fig. 5(a), the symbols represent the experimentally obtained $\Delta\widetilde{G}(B)$ data in the low-field region below 50 K and the corresponding lines are the fitting curves using Eq. (4). The agreement between the theoretical fitting and the experimental data is good, indicating that the MR behaviors can be described by the HLN model. The variation of the fitting parameters α and l_φ with temperature is shown in Fig. 5(b). If the fitting parameter α is close to –0.5, it could be concluded that the WAL effect originates from 2D surface states. However, the value of obtained α is of the order of 10^2, much larger than that of 2D systems. Similar results have been observed in several 3D topological materials such as LuPdBi, ScPtBi, YbCdGe, YbCdSn, CaAgBi, and ScPdBi [30–35], which are attributed to

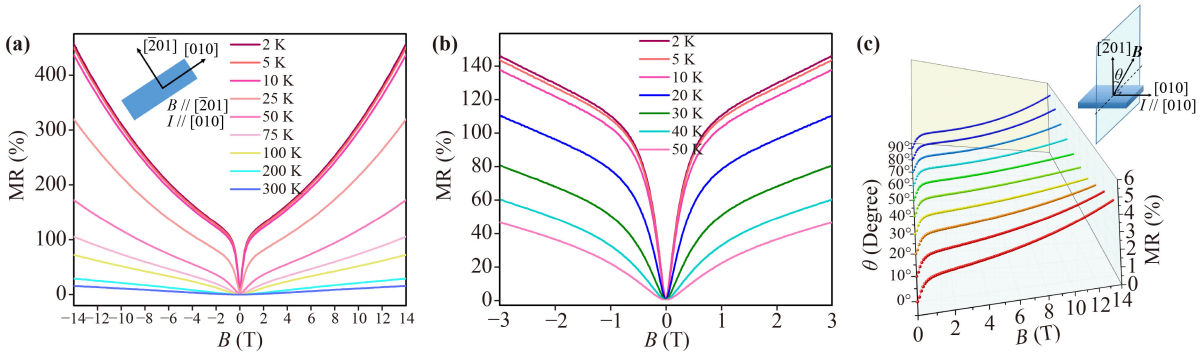

Fig. 4 **(a)** MR plotted as a function of the magnetic field B at different fixed temperatures for the $Ta_{0.7}Nb_{0.3}Sb_2$ single crystal. **(b)** A zoom-in MR measurements below 50 K ranging from –3 T to 3 T. **(c)** MR plotted as a function of the magnetic field at various angles θ at T = 2 K. Insets: Schematic diagrams of the directions of the magnetic field, electric current and crystallographic orientation during different types of MR measurements.

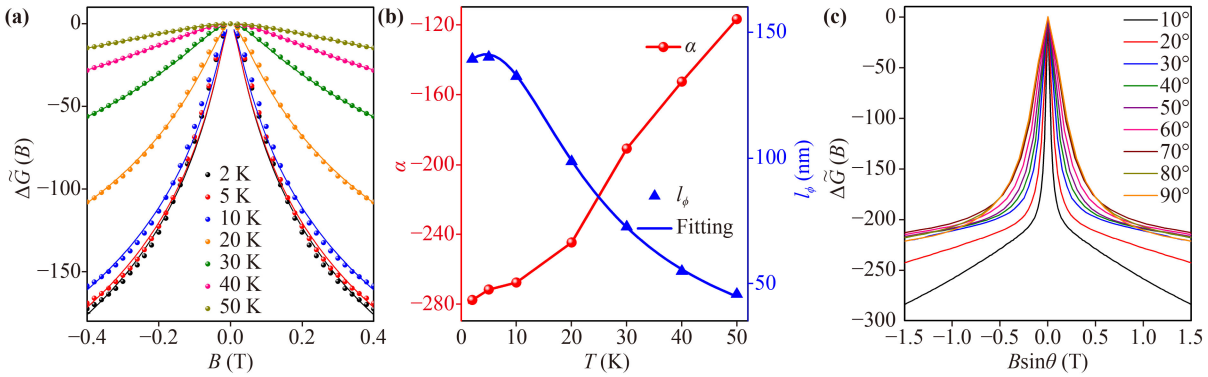

Fig. 5 **(a)** Magnetoconductance $\Delta\widetilde{G}$ as a function of the magnetic field. The solid lines are the fitting results using HLN model. **(b)** Temperature dependence of the parameter α and the phase coherence length l_ϕ, extracted from the HLN model. The solid blue line is the fitting curve using equation (5). **(c)** Angular dependence of the magnetoconductance as a function $B\sin\theta$, as measured at $T = 2$ K.

the dominance of 3D bulk conducting channels rather than 2D surface states. These results imply that the WAL effect in the $Ta_{0.7}Nb_{0.3}Sb_2$ crystal is mainly derived from three-dimension bulk contribution. The value of α shows gentle change in the temperature region 2 K $\leq T \leq$ 10 K, which implies that the number of conductive channels is roughly independent of temperature at very low temperature. As the temperature increases further, the value of α decreases significantly, implying a weakening of the WAL effect with increasing temperature, which corresponds to the decrease in the magnetoconductance in Fig. 5(a).

On the other hand, considering the electron–phonon scattering and the electron–electron interaction, the phase coherence length l_ϕ can be fitted by the following formula:

$$\frac{1}{l_\phi^2(T)} = \frac{1}{l_\phi^2(0)} + A_{ee}T + A_{ep}T^2. \tag{5}$$

Here, $l_\phi(0)$ is the phase coherence length at zero temperature, and $A_{ee}T$ and $A_{ep}T^2$ are the electron-electron and electron-phonon interactions, respectively. In Fig. 5(b), the blue solid triangle symbols are the value of $l_\phi(T)$ which is obtained by fitting $\Delta\widetilde{G}(B)$ in Fig. 5(a) using Eq. (4) and the solid line shows the fitting curves of $l_\phi(T)$ vs. T using equation (5). The best fitting yield $l_\phi(0) = 136$ nm, $A_{ee} = -1.79 \times 10^{-6}(\text{nm}^2 \cdot \text{K})^{-1}$, $A_{ep} = 2.13 \times 10^{-7}(\text{nm}^2 \cdot \text{K}^2)^{-1}$, which indicates that the electron-electron scattering is more significant than electron-phonon scattering.

To further confirm the origin of the WAL effect in the $Ta_{0.7}Nb_{0.3}Sb_2$ single crystal, we carried out MR measurements by rotating the direction of the magnetic field with respect to the electric current at $T = 2$ K, and calculated the corresponding $\Delta\widetilde{G}$. Figure 5(c) shows the variation of $\Delta\widetilde{G}$ with the normal component of the external magnetic field $B\sin\theta$, where θ is the angle between the direction of the magnetic field and $[\bar{2}01]$ orientation. If the WAL is caused by 2D surface states, the $\Delta\widetilde{G}$ vs. $B\sin\theta$ curves should merge into a universal curve, suggesting that the magnetoconductance depends mainly on the perpendicular component of the applied magnetic fields [24, 27, 34]. As shown in Fig. 5(c), however, the nine curves with different tilt angles θ do not coincide with each other, confirming the WAL effect in the bulk single crystal of $Ta_{0.7}Nb_{0.3}Sb_2$ mainly results from the contribution of 3D bulk transport [35–38]. This conclusion is consistent with the relatively large α value discussed above.

Figures 4(c) and 5(c) show the MR curves at different angle θ at 2 K, from which the anisotropy of MR under different magnetic fields can be observed. To show this anisotropic MR behaviors more clearly, we conducted angular dependent MR (AMR) measurements at 2 K under various magnetic fields and show the results in Fig. 6. Note that the starting point (0°) means that the direction of the magnetic field is along the $[\bar{2}01]$ crystallographic direction. During the rotation of the crystal, the direction of the magnetic field always keeps perpendicular to the direction of the electric current which is along the [010] direction of the crystal. The rotation is asymmetric near 0°, where the positive direction rotates towards [001] direction, and the negative direction rotates towards [100] direction. In the low-field region [Figs. 6(a)–(d)], the maximum MR is obtained at $\theta \approx$ –30°–35°, where the magnetic field is roughly along the [100] crystallographic direction. An interesting point is that the minimum MR is observed at $\theta = 90°$, where the magnetic field is not along the [001] axis, therefore resulting in a twisted figure of "8" shaped AMR. As discussed above, the WAL effect dominates the MR behaviors at low magnetic fields. That is to say, the AMR in the low magnetic-field regions mainly reflects the WAL's contribution to MR. The WAL usually follows cosine rule or close-to-cosine rule during rotation, which leads to two-fold symmetrical AMR. As a result, the AMRs in Figs. 6(a)–(d) shows a two-fold rotational symmetry in a shape of "8". In high magnetic fields ($B \geq 2$ T), MR shows the maximum for the direction of

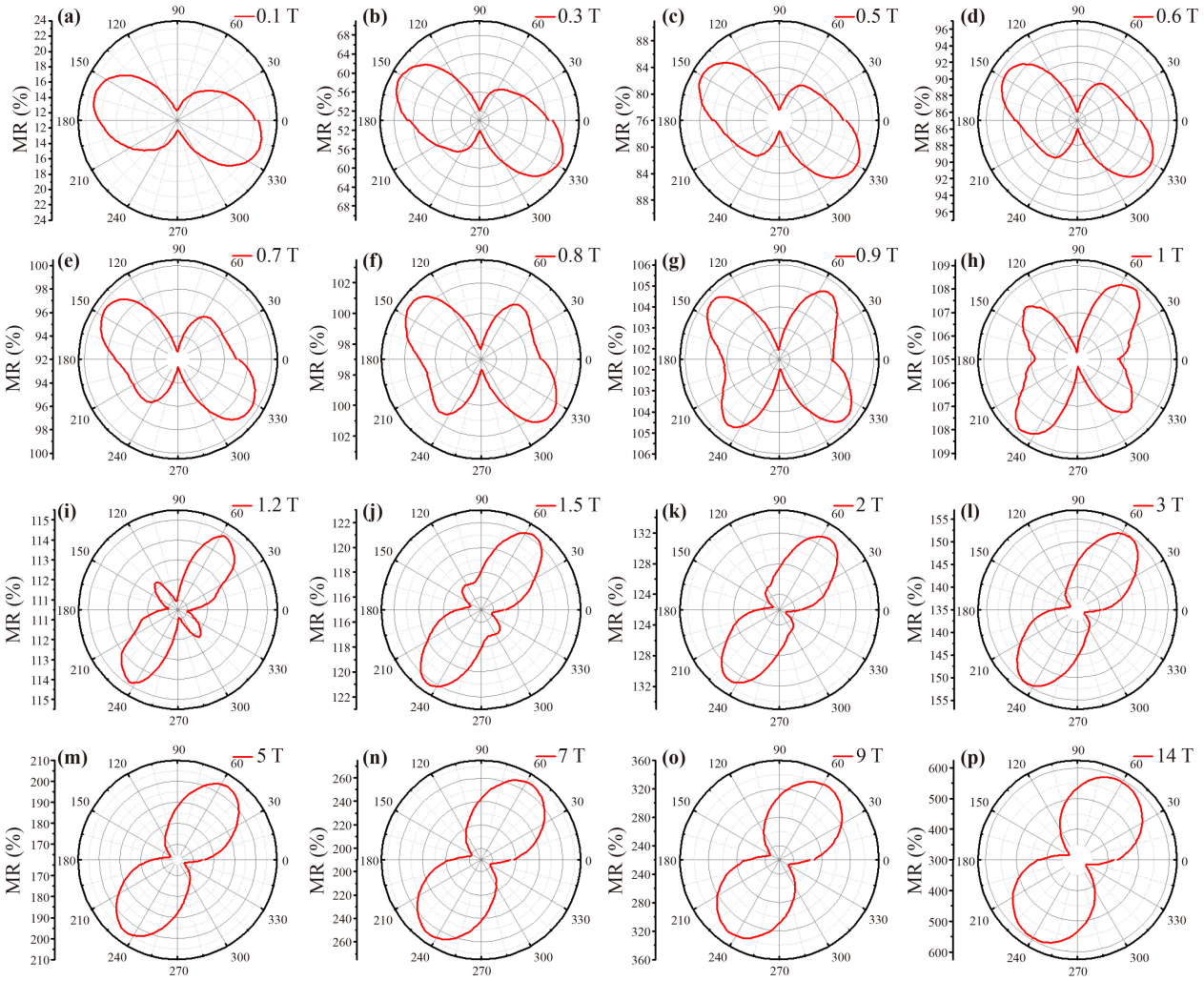

Fig. 6 Angular dependent MR at $T = 2$ K and various magnetic fields for the $Ta_{0.7}Nb_{0.3}Sb_2$ single crystal.

the magnetic field along the [001] direction of the crystal, while it shows the minimum for the direction of the magnetic field along the [100] direction, also resulting in a figure of "8" shaped AMR. The WAL effect is greatly inhibited by high magnetic fields. Therefore, these two-fold-rotation symmetric patterns at high magnetic fields ($B \geq 2$T) may be due to the intrinsic geometry of Fermi pockets and their relative contribution to electronic transports [11, 51, 52, 53]. Both in low field limits and high field limits, the AMR are two-fold symmetry or roughly two-fold symmetry, however, the maximum MR appears at different angle θ. For low field limit, the maximum MR appears at θ = –30°–35° [Figs. 6(a)–(d)] while for the high field limit the maximum MR appears at θ = 60° [e.g., Fig. 6(p)] Therefore, upon increasing the magnetic field, the angle (θ) where the maximum MR appears would rotate. As shown in Figs. 6(f)–(i), in the intermediate field range (0.8 T $\leq B \leq$ 1.5 T), the AMR shows roughly four-fold symmetry, which probably originates from the competition of the low-field WAL dominated MR with the high-field fermiology dominated MR.

4 Conclusions

We report the magnetotransport properties of high quality $Ta_{0.7}Nb_{0.3}Sb_2$ single crystals. The crystals show metallic electronic transport behaviors and resistivity plateaus under magnetic fields as well as magnetic-field-induced resistivity upturn upon cooling. Hall measurements and two-band model fitting results indicate that the crystals show off-compensation of electron and hole carrier density at low temperatures [8 (electrons): 1 (holes)] and high mobility (> 1000 $cm^2 \cdot V^{-1} \cdot s^{-1}$) in the 2 –300 K region. One interesting finding is that the WAL effect can be observed up to 50 K, which results from the strong SOC in 3D bulk, and a large MR of 120% is obtained at B = 1 T and T = 2 K. The fitting of temperature dependent l_ϕ demonstrates that the predominant scattering mechanism is the electron-electron scattering. The low-field WAL at $T = 2$ K shows angular dependence behaviors, and MR value reaches its maximum when the magnetic field is along the [100] crystallographic direction. Another interesting finding is the change of the symmetry of AMR from two-fold (≤ 0.6 T) to

four-fold (0.8 –1.5 T) and finally to two-fold (≥ 2 T), which is attributed to the evolution of the mechanism from the low-field WAL dominated MR to WAL and fermiology co-dominated MR and finally to high-field fermiology dominated MR.

Acknowledgements This work was supported by the National Natural Science Foundation of China (Grant Nos. 11974155 and 12104128), the Natural Science Foundation of Jiangsu Province (Grant No. BK20210360), the Postdoctoral Research Program of Jiangsu Province (Grant No. 2021K581C), and the Fundamental Research Funds for the Central Universities (Grant No. B210201026). W. Z. and X. W. acknowledge the support from ARC Centre of Excellence in Future Low-Energy Electronic Technologies (No. CE170100039).

References

1. M. Z. Hasan and C. L. Kane, Colloquium: Topological insulators, *Rev. Mod. Phys.* 82(4), 3045 (2010)
2. M. He, H. Sun, and Q. L. He, Topological insulator: Spintronics and quantum computations, *Front. Phys.* 14(4), 43401 (2019)
3. B. Yan and C. Felser, Topological materials: Weyl semimetals, *Annu. Rev. Condens. Matter Phys.* 8(1), 337 (2017)
4. B. Keimer and J. E. Moore, The physics of quantum materials, *Nat. Phys.* 13(11), 1045 (2017)
5. Y. Tokura, K. Yasuda, and A. Tsukazaki, Magnetic topological insulators, *Nat. Rev. Phys.* 1(2), 126 (2019)
6. H. P. Sun and H. Z. Lu, Quantum transport in topological semimetals under magnetic fields (II), *Front. Phys.* 14(3), 33405 (2019)
7. L. Guo, Y. K. Liu, G. Y. Gao, Y. Y. Huang, H. Gao, L. Chen, W. Zhao, W. Ren, S. Y. Li, X. G. Li, S. Dong, and R. K. Zheng, Extreme magnetoresistance and SdH oscillation in compensated semimetals of $NbSb_2$ single crystals, *J. Appl. Phys.* 123(15), 155103 (2018)
8. Y. Zhou, C. Gu, X. Chen, Y. Zhou, C. An, and Z. Yang, Structural and transport properties of the topological semimetal $TaSb_2$ at high pressures, *J. Solid State Chem.* 265, 359 (2018)
9. K. Wang, D. Graf, L. Li, L. Wang, and C. Petrovic, Anisotropic giant magnetoresistance in $NbSb_2$, *Sci. Rep.* 4(1), 7328 (2015)
10. Y. Li, L. Li, J. Wang, T. Wang, X. Xu, C. Xi, C. Cao, and J. Dai, Resistivity plateau and negative magnetoresistance in the topological semimetal $TaSb_2$, *Phys. Rev. B* 94(12), 121115(R) (2016)
11. A. Pariari, R. Singha, S. Roy, B. Satpati, and P. Mandal, Anisotropic transverse magnetoresistance and Fermi surface in $TaSb_2$, *Sci. Rep.* 8(1), 10527 (2018)
12. L. Guo, M. Xu, L. Chen, X. Huang, X. Y. Shi, J. S. Ying, T. Zhang, W. Zhao, S. Dong, and R. K. Zheng, Electronic transport properties of $Nb_{1-x}Ta_xSb_2$ single-crystal semimetals grown by a chemical vapor transport based high-throughput method, *Cryst. Growth Des.* 21(1), 653 (2021)
13. D. Gresch, Q. Wu, G. W. Winkler, and A. A. Soluyanov, Hidden Weyl points in centrosymmetric paramagnetic metals, *New J. Phys.* 19(3), 035001 (2017)
14. C. Xu, J. Chen, G. X. Zhi, Y. Li, J. Dai, and C. Cao, Electronic structures of transition metal dipnictides XPn_2(X = Ta, Nb; Pn = P, As, Sb), *Phys. Rev. B* 93(19), 195106 (2016)
15. I. Belopolski, D. S. Sanchez, Y. Ishida, X. C. Pan, P. Yu, S. Y. Xu, G. Q. Chang, T. R. Chang, H. Zheng, N. Alidoust, G. Bian, M. Neupane, S. M. Huang, C. C. Lee, Y. Song, H. Bu, G. Wang, S. Li, G. Eda, H. T. Jeng, T. Kondo, H. Lin, Z. Liu, F. Song, S. Shin, and M. Z. Hasan, Discovery of a new type of topological Weyl fermion semimetal state in $Mo_xW_{1-x}Te_2$, *Nat. Commun.* 7(1), 13643 (2016)
16. T. R. Chang, S. Y. Xu, G. Chang, C. C. Lee, S. M. Huang, B. K. Wang, G. Bian, H. Zheng, D. S. Sanchez, I. Belopolski, N. Alidoust, M. Neupane, A. Bansil, H. T. Jeng, H. Lin, and M. Z. Hasan, Prediction of an arc-tunable Weyl Fermion metallic state in $Mo_xW_{1-x}Te_2$, *Nat. Commun.* 7(1), 10639 (2016)
17. Y. Wang, E. Liu, H. Liu, Y. Pan, L. Zhang, J. Zeng, Y. Fu, M. Wang, K. Xu, Z. Huang, Z. Wang, H. Z. Lu, D. Xing, B. Wang, X. Wan, and F. Miao, Gate-tunable negative longitudinal magnetoresistance in the predicted type-II Weyl semimetal WTe_2, *Nat. Commun.* 7(1), 13142 (2016)
18. H. Liu, S. Liu, Y. Yi, H. He, and J. Wang, Shubnikov–de Haas oscillations in n and p type Bi_2Se_3 flakes, *2D Mater.* 2(4), 045002 (2015)
19. Y. Xing, Y. Sun, M. Singh, Y. F. Zhao, M. H. W. Chan, and J. Wang, Electronic transport properties of topological insulator films and low dimensional superconductors, *Front. Phys.* 8(5), 491 (2013)
20. A. Laitinen, M. Kumar, and P. J. Hakonen, Weak antilocalization of composite fermions in graphene, *Phys. Rev. B* 97(7), 075113 (2018)
21. M. Jenderka, J. Barzola-Quiquia, Z. Zhang, H. Frenzel, M. Grundmann, and M. Lorenz, Mott variable-range hopping and weak antilocalization effect in heteroepitaxial Na_2IrO_3 thin films, *Phys. Rev. B* 88(4), 045111 (2013)
22. M. Xu, T. W. Chen, J. M. Yan, L. Guo, H. Wang, G. Y. Gao, H. S. Luo, Y. Chai, and R. K. Zheng, Tunable magnetoresistance and charge carrier density in Cr: In_2O_3/$PbMg_{1/3}Nb_{2/3}O_3$–$PbTiO_3$ ferroelectric field-effect devices, *Phys. Rev. Appl.* 13(6), 064006 (2020)
23. Y. Gan, J. Liang, C. Cho, S. Li, Y. Guo, X. Ma, X. Wu, J. Wen, X. Du, M. He, C. Liu, S. A. Yang, K. Wang, and L. Zhang, Bandgap opening in $MoTe_2$ thin flakes induced by surface oxidation, *Front. Phys.* 15(3), 33602 (2020)
24. K. Shrestha, M. Chou, D. Graf, H. D. Yang, B. Lorenz, and C. W. Chu, Extremely large nonsaturating magnetoresistance and ultrahigh mobility due to topological surface states in the metallic Bi_2Te_3 topological insulator, *Phys. Rev. B* 95(19), 195113 (2017)
25. O. Chiatti, C. Riha, D. Lawrenz, M. Busch, S. Dusari, J. Sanchez-Barriga, A. Mogilatenko, L. V. Yashina, S. Valencia, A. A. Unal, O. Rader, and S. F. Fischer, 2D layered transport properties from topological insulator Bi_2Se_3 single crystals and micro flakes, *Sci. Rep.* 6(1), 27483 (2016)
26. C. Shekhar, C. E. ViolBarbosa, B. Yan, S. Ouardi, W.

Schnelle, G. H. Fecher, and C. Felser, Evidence of surface transport and weak antilocalization in a single crystal of the Bi_2Te_2Se topological insulator, *Phys. Rev. B* 90(16), 165140 (2014)
27. K. Shrestha, D. Graf, V. Marinova, B. Lorenz, and C. W. Chu, Weak antilocalization effect due to topological surface states in $Bi_2Se_{2.1}Te_{0.9}$, *J. Appl. Phys.* 122(14), 145901 (2017)
28. W. Zhao, L. Chen, Z. Yue, Z. Li, D. Cortie, M. Fuhrer, and X. Wang, Quantum oscillations of robust topological surface states up to 50 K in thick bulk-insulating topological insulator, *npj Quantum Mater.* 4(1), 56 (2019)
29. G. Xu, W. Wang, X. Zhang, Y. Du, E. Liu, S. Wang, G. Wu, Z. Liu, and X. X. Zhang, Weak antilocalization effect and noncentrosymmetric superconductivity in a topologically nontrivial semimetal LuPdBi, *Sci. Rep.* 4(1), 5709 (2015)
30. O. Pavlosiuk, D. Kaczorowski, and P. Wisniewski, Shubnikov–de Haas oscillations, weak antilocalization effect and large linear magnetoresistance in the putative topological superconductor LuPdBi, *Sci. Rep.* 5(1), 9158 (2015)
31. Z. Hou, Y. Wang, E. Liu, H. Zhang, W. Wang, and G. Wu, Large low-field positive magnetoresistance in nonmagnetic half-Heusler ScPtBi single crystal, *Appl. Phys. Lett.* 107(20), 202103 (2015)
32. A. Laha, S. Malick, R. Singha, P. Mandal, P. Rambabu, V. Kanchana, and Z. Hossain, Magnetotransport properties of the correlated topological nodal-line semimetal YbCdGe, *Phys. Rev. B* 99(24), 241102(R) (2019)
33. A. Laha, P. Rambabu, V. Kanchana, L. Petit, Z. Szotek, and Z. Hossain, Experimental and theoretical study of the correlated compound YbCdSn: Evidence for large magnetoresistance and mass enhancement, *Phys. Rev. B* 102(23), 235135 (2020)
34. S. Sasmal, R. Mondal, R. Kulkarni, A. Thamizhavel, and B. Singh, Magnetotransport properties of noncentrosymmetric CaAgBi single crystal, *J. Phys.: Condens. Matter* 32(33), 335701 (2020)
35. J. Zhang, Z. Hou, C. Zhang, J. Chen, P. Li, Y. Wen, Q. Zhang, W. Wang, and X. Zhang, Weak antilocalization effect and high-pressure transport properties of ScPdBi single crystal, *Appl. Phys. Lett.* 115(17), 172407 (2019)
36. L. Deng, Z. H. Liu, X. Q. Ma, Z. P. Hou, E. K. Liu, X. K. Xi, W. H. Wang, G. H. Wu, and X. X. Zhang, Observation of weak antilocalization effect in high-quality ScNiBi single crystal, *J. Appl. Phys.* 121(10), 105106 (2017)
37. J. Chen, H. Li, B. Ding, Z. Hou, E. Liu, X. Xi, H. Zhang, G. Wu, and W. Wang, Structural and magnetotransport properties of topological trivial LuNiBi single crystals, *J. Alloys Compd.* 784, 822 (2019)
38. Z. Hou, Y. Wang, G. Xu, X. Zhang, E. Liu, W. Wang, Z. Liu, X. Xi, W. Wang, and G. Wu, Transition from semiconducting to metallic-like conducting and weak antilocalization effect in single crystals of LuPtSb, *Appl. Phys. Lett.* 106(10), 102102 (2015)
39. S. Hikami, A. I. Larkin, and Y. Nagaoka, Spin–orbit interaction and magnetoresistance in the two dimensional random system, *Prog. Theor. Phys.* 63(2), 707 (1980)
40. B. A. Assaf, T. Cardinal, P. Wei, F. Katmis, J. S. Moodera, and D. Heiman, Linear magnetoresistance in topological insulator thin films: Quantum phase coherence effects at high temperatures, *Appl. Phys. Lett.* 102(1), 012102 (2013)
41. A. Rehr and S. M. Kauzlarich, $NbSb_2$, *Acta Crystallogr. C* 50(8), 1177 (1994)
42. R. Singha, A. K. Pariari, B. Satpati, and P. Mandal, Large nonsaturating magnetoresistance and signature of nondegenerate Dirac nodes in ZrSiS, *Proc. Natl. Acad. Sci. USA* 114(10), 2468 (2017)
43. S. Sun, Q. Wang, P. J. Guo, K. Liu, and H. Lei, Large magnetoresistance in LaBi: Origin of field-induced resistivity upturn and plateau in compensated semimetals, *New J. Phys.* 18(8), 082002 (2016)
44. F. F. Tafti, Q. D. Gibson, S. K. Kushwaha, N. Haldolaarachchige, and R. J. Cava, Resistivity plateau and extreme magnetoresistance in LaSb, *Nat. Phys.* 12(3), 272 (2016)
45. L. Guo, T. W. Chen, C. Chen, L. Chen, Y. Zhang, G. Y. Gao, J. Yang, X. G. Li, W. Y. Zhao, S. Dong, and R. K. Zheng, Electronic transport evidence for topological nodal-line semimetals of ZrGeSe single crystals, *ACS Appl. Electron. Mater.* 1(6), 869 (2019)
46. J. M. Ziman, Electrons and Phonons: The Theory of Transport Phenomena in Solids, Oxford University Press, 1960
47. Y. L. Wang, L. R. Thoutam, Z. L. Xiao, J. Hu, S. Das, Z. Q. Mao, J. Wei, R. Divan, A. Luican-Mayer, G. W. Crabtree, and W. K. Kwok, Origin of the turn-on temperature behavior in WTe_2, *Phys. Rev. B* 92(18), 180402(R) (2015)
48. Y. Kopelevich, J. C. M. Pantoja, R. R. da Silva, and S. Moehlecke, Universal magnetic-field-driven metal–insulator–metal transformations in graphite and bismuth, *Phys. Rev. B* 73(16), 165128 (2006)
49. C. M. Hurd, The Hall Effect in Metals and Alloys, Plenum, New York, 1972
50. H. T. He, G. Wang, T. Zhang, I. K. Sou, G. K. L. Wong, J. N. Wang, H. Z. Lu, S. Q. Shen, and F. C. Zhang, Impurity effect on weak antilocalization in the topological insulator Bi_2Te_3, *Phys. Rev. Lett.* 106(16), 166805 (2011)
51. Z. Yuan, H. Lu, Y. Liu, J. Wang, and S. Jia, Large magnetoresistance in compensated semimetals $TaAs_2$ and $NbAs_2$, *Phys. Rev. B* 93(18), 184405 (2016)
52. A. Collaudin, B. Fauqué, Y. Fuseya, W. Kang, and K. Behnia, Angle dependence of the orbital magnetoresistance in Bismuth, *Phys. Rev. X* 5(2), 021022 (2015)
53. Y. Luo, R. D. McDonald, P. F. S. Rosa, B. Scott, N. Wakeham, N. J. Ghimire, E. D. Bauer, J. D. Thompson, and F. Ronning, Anomalous electronic structure and magnetoresistance in $TaAs_2$, *Sci. Rep.* 6(1), 27294 (2016)